DOI: 10.1038/s41561-020-00656-2 https://www.nature.com/articles/s41561-020-00656-2

# Increased typhoon activity in the Pacific deep tropics driven by Little Ice Age circulation changes

**James F. Bramante[1,2]*, Murray R. Ford[3], Paul S. Kench[4], Andrew D. Ashton[1], Michael R. Toomey[5], Richard Sullivan[1], Kristopher B. Karnauskas[6], Caroline C. Ummenhofer[7], Jeffrey P. Donnelly[1]**

[1]Department of Geology and Geophysics, Woods Hole Oceanographic Institution, Woods Hole, MA 02543, USA
[2]Department of Earth, Atmospheric, and Planetary Sciences, Massachusetts Institute of Technology, Cambridge, MA 02139, USA
[3]School of Environment, The University of Auckland, Auckland 1142, New Zealand
[4]Department of Earth Sciences, Simon Fraser University, BC V5A 1S6, Canada
[5]U.S. Geological Survey, Florence Bascom Geoscience Center, Reston, VA 20192, USA
[6]Department of Atmospheric and Ocean Sciences, University of Colorado, Boulder, CO 80309, USA
[7]Department of Physical Oceanography, Woods Hole Oceanographic Institution, Woods Hole, MA 02543, USA
*Corresponding author. e-mail: James.F.Bramante@gmail.com

**The instrumental record reveals that tropical cyclone activity is sensitive to oceanic and atmospheric variability on inter-annual and decadal scales. However, our understanding of climate's influence on tropical cyclone behavior is restricted by the short historical record and the sparseness of prehistorical reconstructions, particularly in the western North Pacific where coastal communities suffer loss of life and livelihood from typhoons annually. Here, to explore past regional typhoon dynamics, we reconstruct three millennia of deep tropical North Pacific cyclogenesis. Combined with existing records, our reconstruction demonstrates that low baseline typhoon activity prior to 1350 C.E. was followed by an interval of frequent storms during the Little Ice Age. This pattern, concurrent with hydroclimate proxy variability, suggests a centennial-scale link between Pacific hydroclimate and tropical cyclone climatology. An ensemble of global climate models demonstrates a migration of the Pacific Walker circulation and variability in two Pacific climate modes during the Little Ice Age that likely contributed to enhanced tropical cyclone activity in the tropical western North Pacific. Looking**

**towards the next century, projected changes to the Pacific Walker Circulation and expansion of the tropics invert these Little Ice Age hydroclimate trends, potentially reducing typhoon activity in the deep tropical Pacific.**

Determining the hazard risk of coastal communities as climate changes requires an understanding of the influence of climate variability on tropical cyclone (TC) activity. From 2010 to 2030, global population growth is estimated to increase the number of people exposed annually to TCs from 133.7 million to 149.3 million, 90% of whom live along the Asian Pacific coastline[1]. Simultaneously, anthropogenic forcing is expected to alter global climate, affecting the frequency, geographic distribution, and intensity of TC's[2,3]. However, the influence of global climate is mediated by regional climate characteristics varying on seasonal to centennial timescales[4-8]. Understanding the mechanisms by which TCs have varied in response to past forcing will help us understand how TC risk might change with continued anthropogenic radiative forcing.

Our understanding of climate controls on TCs is limited by the observational record. The western North Pacific (WNP) is the most active basin for TCs globally, yet few pre-modern reconstructions with annual-decadal resolution have been developed there[9-11] relative to the western North Atlantic[6,12-16]. This dearth of WNP TC reconstructions hinders identification of the internal and external processes that drive low-frequency variability in TC statistics. As TCs travel, they are influenced by variable environmental conditions along their tracks[2].,Separating the influence of different aggregate TC characteristics (i.e. genesis frequency, genesis location, storm track, and landfall intensity) on reconstructed variability is difficult when a reconstruction is located far from genesis locations. In the western North Atlantic, recent research has overcome this difficulty by contrasting records at many sites across the basin, revealing that regional ocean circulation likely altered the dominant storm track, in turn driving a cross-basin shift in TC landfall frequency from the Gulf of Mexico to the northeastern USA about 550 cal. yr BP[6,12]. In the WNP, however, the few TC reconstructions that exist are located far from the primary cyclogenesis regions. Thus, attempts to contrast records on the western basin margin have failed to identify the TC characteristics and drivers responsible for a clear southward shift in landfall frequency 500 cal. yr BP[9,17], for example.

Here we introduce a sediment proxy reconstruction of TC landfall frequency that captures genesis variability in the deep tropical central Pacific—a hotspot of tropical cyclogenesis that feeds the WNP basin. Tropical cyclogenesis potential in the WNP is expected to increase with warming sea surface temperatures (SST) and weakening of vertical wind shear (VWS) projected over the 21st century[18]. The proximity between genesis location and proxy site mitigates the influence of storm track and post-genesis intensification on our reconstruction. By focusing on TC genesis and using a multi-model ensemble of general circulation models (GCMs), we can identify the climate patterns influencing cyclogenesis variability near our site.

**Tropical cyclone genesis over the past 3,000 years**

We developed a grain-size proxy of cross-reef sediment transport intensity from a sediment core retrieved from a blue hole, a 30 m deep karst basin, on Jaluit Atoll (6.256°N, 169.411°E, ED Fig. 1). Coastal basins preserve evidence of the close passage of intense TCs as anomalously coarse layers of sediment[13,15]. We sieved the core sediment and identified TC deposits as peaks in the sediment coarse fraction (250-2,000 µm sieve diameter) that exceeded a statistical threshold (see Methods). A post-bomb radiocarbon date indicates that the youngest coarse layer was deposited in the late 1950s and probably by Typhoon Ophelia in 1958, which passed directly over Jaluit with estimated sustained winds of over 64 $ms^{-1}$ (nearly a super typhoon, or Category 4 on the Saffir-Simpson scale) causing widespread destruction[19]. The coarse fraction anomalies of all identified event beds are close to or exceed that of Ophelia, suggesting that the frequency of coarse deposits in our core corresponds to the frequency of intense TC passage near Jaluit over the past c. 3,000 years. Due to the position of the site southeast of the WNP basin, near the geographical limits of observed tropical cyclogenesis, we interpret temporal variability in our record as directly corresponding to temporal variability in nearby cyclogenesis (see Supplementary Discussion).

Our reconstruction of centennial TC frequency displays a mean of 1 event/century and centennial variability similar to other reconstructions from the western Pacific. The most prominent feature in our record is a peak in frequency c. 1350-1700 CE with a maximum of 3.75 events/century that encompasses the early Little Ice Age (LIA, 1400-1700 CE), is higher than during any other period (Fig. 1e), and is unlikely to be the product of unforced variability (Methods). Immediately preceding the LIA peak was a relatively quiet interval encompassing the Medieval Climate Anomaly (MCA, 1000-1300 CE). The LIA peak in cyclogenesis at Jaluit is synchronous with a substantial increase in the frequency of coarse deposits at Yongshu Reef in a South China Sea (SCS) sediment core, indicating enhanced landfall frequency relative to the MCA[11], and enhanced landfall frequency in Guangdong Province according to Chinese historical records[10] (Fig. 1c,d). A sedimentary reconstruction of TC landfall on Tahaa, French Polynesia recorded few storms over the past 1000 years[20], but reef-top storm deposits collected from across the central South Pacific basin suggest higher TC activity during the MCA than the LIA[21,22] (Fig. 1a,b).

**Large-scale drivers of tropical cyclone variability**

In the instrumental record, the El Nino Southern Oscillation (ENSO) dominates inter-annual variability in western Pacific cyclogenesis. During El Nino events, the mean TC genesis location in the WNP shifts to the southeast, and TCs tend to recurve north more than in non-event years[23,24]. Thus, El Nino events result in more frequent cyclogenesis near Jaluit, but fewer storm tracks crossing the SCS near Yongshu Reef[24]. In the South Pacific, El Nino events tend to shift the mean genesis location eastward, resulting in fewer cyclone landfalls in Australia, but more in the central South Pacific and French Polynesia[21,25]. These effects scale with the intensity of ENSO-associated SST anomalies and are more sensitive to central Pacific warming than eastern Pacific El Nino events[24].

Given the dominant influence of ENSO on cyclogenesis in the WNP historically, variations in ENSO over the past few millennia could have contributed to the variability in our reconstruction. A synthesis of annually-resolved SST proxies for the Nino3.4 region[26] demonstrates that SST variability associated with ENSO was lower over much of the last millennium relative to the last century (Fig. 2a). However, over this background signal there were two century-long periods of elevated ENSO variability that correspond with the beginning and end of the active interval in our record. Additionally, an annually-resolved reconstruction of SSTs in the Nino4 region from Taiwanese tree ring $\delta^{18}O$ reveals a peak in ENSO-associated variability c. 1350-1425 CE, during peak cyclogenesis in our reconstruction[27]. Coral-based SST proxies from the central Pacific detail similar, but shorter-duration fluctuations in ENSO variability during the LIA[28] (Fig. 2b). These transient peaks in ENSO-associated SST variability imply more frequent or more intense El Nino events, either of which would have increased the frequency of TC cyclogenesis near Jaluit and thus likely increased the frequency of TCs in our record.

However, the SST reconstructions also indicate that ENSO-associated variability was higher during the last century than during the LIA, contrary to cyclogenesis in our reconstruction. Additionally, the enhanced frequency or magnitude of El Nino events suggested by peaks in ENSO-associated variability cannot explain enhanced landfall frequency near Yongshu Reef and the absence of an increase in TC activity in the central South Pacific during the LIA. Thus, it is likely that other factors contributed substantially to cyclogenesis variability over the last millennium.

Hydroclimate proxies from the Indo-Pacific Warm Pool (IPWP) and the central and eastern Pacific demonstrate rapid, synchronous, and spatially consistent change at the onset of the LIA. Around 1400 CE, $\delta^{18}O$ records from speleothems in northwestern Australia and southern China demonstrate a rapid transition to a drier climate that lasted to c. 1750 CE[29] (Fig. 2e). Simultaneously, precipitation proxies in the deep tropical IPWP and SCS indicate the rapid onset of wetter climate[30,31]. These shifts have been attributed to contraction of the Intertropical Convergence Zone (ITCZ)[29,31] (Fig. 2e) and a westward shift in the Pacific Walker Circulation (PWC)[30]. Simultaneously, an algal lipid δD record indicates the rapid onset of dry conditions in the central North Pacific[32] (Fig. 2c), and enhanced ice accumulation in Quelccaya ice cap, Peru[33] (Fig. 2d) indicates wetter conditions in the eastern South Pacific. These meridional shifts in precipitation have been attributed to a southward displacement of the ITCZ during the LIA. A radiocarbon date from 5 cm above the first event layer in the LIA active interval constrains its modeled age distribution to overlap with the onset of these changes in hydroclimate proxies in the Pacific (Fig. 2g). Thus, the start of the LIA active interval may have been concurrent with the basin-wide transitions between wet and dry conditions.

The tropical atmospheric circulation patterns driving hydroclimate variability during the LIA could have influenced cyclogenesis across the western Pacific. Contraction of the ITCZ would entail contraction in the Hadley circulation, which dictates the characteristics (latitude, width, intensity) of zonal mean precipitation in the tropics. Recent research suggests tropical cyclogenesis in the WNP shifted to the north over the past few decades as the Hadley cell expanded poleward due to anthropogenic climate change[34,35]. Assuming Hadley cell contraction would have the opposite effect, the LIA contraction could have enhanced cyclogenesis in the deep tropics (0-10°N) near Jaluit. Alternatively, inter-annual variability in the Pacific Meridional Mode (PMM) has influenced PWC and correlated with zonal shifts in WNP cyclogenesis over the past few decades[7,36]. Thus, westward migration of the rising limb of the PWC could have shifted cyclogenesis westward during the LIA as well.

## Detection of climatic drivers in a climate model ensemble

To explore the associations between tropical atmospheric circulation and temporal variability in our reconstruction, we analyzed the results of the last millennium experiment in an ensemble of Coupled Model Intercomparison Project phase 5 (CMIP5) GCMs. By diagnosing a genesis potential index (GPI)[37,38] from monthly-mean climate model output we determined that the ensemble predicted cyclogenesis anomalies during the LIA relative to the MCA that were consistent with TC reconstructions across the tropical WNP (Fig. 3a). The ensemble indicated anomalously high GPI in the vicinity of the Philippines. Assuming TCs entering the SCS are generated primarily to the east and southeast, these results are consistent with the Yongshu Reef proxy reconstruction[11] and historical records from Guangdong[10], both of which recorded enhanced TC activity during the LIA relative to the MCA (Fig. 1d). In the near-equatorial central North Pacific where most TCs recorded at Jaluit originate, the ensemble showed patchy positive GPI anomalies, while GPI was reduced directly over Jaluit. However, wind shear (potential intensity) decreased (increased) near our site with a relatively unchanged mid-troposphere entropy gradient (ED Fig. 6c-e), indicating that TCs generated in the positive GPI anomalies would continue intensification over Jaluit, despite the lower GPI driven by anomalously low ambient vorticity. Additionally, El Nino events occurring in this centennial mean state would likely increase vorticity[39] and decrease the moist entropy gradient[24], further enhancing GPI over Jaluit. However, the lack of inter-model agreement in the equatorial region for GPI and its individual components suggests that the anomalies there may not be a robust response to consistent forcing.

Spatially coherent shifts in environmental conditions generated most of the modeled GPI anomalies during the LIA. An anomalously large mid-troposphere moist entropy deficit across most of the western Pacific suppressed potential cyclogenesis in the models (ED Fig. 6e). However, modeled VWS anomalies were negative (positive) in the western (eastern) half of the basin, promoting (reducing) TC intensification, forming a zonal dipole in the tropics that produced positive GPI anomalies in the SCS and east of the Philippines (Fig. 3b). Indeed, at either end of the tropical WNP the LIA VWS anomaly exceeded the 95% confidence interval of anomalies from all 300-year periods in the last millennium experiment (Fig. 4a) and thus exceeded model background variability. Background variability overwhelmed a similar zonal gradient formed by potential intensity anomalies (Fig. 4b).

Further analysis of the GCM ensemble revealed that the zonal dipole in anomalous VWS was generated by a westward shift in the rising arm of the PWC during the LIA (Fig. 4c,d). In the Last Millennium experiment mean, zonal winds converge at the surface and diverge at height within 130-180°E (Fig. 4c). At either end of the basin, mean zonal winds at the surface and top of the troposphere are opposed, generating high VWS. During the LIA and across the basin, zonal winds became more westerly at the surface and easterly at the top of the troposphere. These wind anomalies weakened (strengthened) shear in the west (east) where they opposed (bolstered) mean wind direction, producing the dipole in VWS anomalies (Fig. 4a). These wind anomalies would also shift the rising limb of PWC westward, consistent with the hypothesized mechanism for a zonal concentration of precipitation in the IPWP[30].

**Influence of climate modes on tropical cyclone variability**

The tropical zonal wind and VWS anomalies during the LIA are associated with centennial variability in PMM. In the instrumental record, PMM is a climate mode second only to ENSO in accounting for interannual variability of east tropical Pacific SST and wind anomalies[40]. Its positive (negative) phase is characterized by strengthened (weakened) meridional SST gradients across the mean latitude of the eastern Pacific ITCZ, northward (southward) shifts in the eastern Pacific ITCZ, and weaker (stronger) trade winds in the eastern North Pacific. Positive (negative) PMM also generates anomalous VWS in the

WNP that causes an eastward (westward) shift in cyclogenesis[7,36]. Positive PMM events often precede and may initiate El Nino events[41], and the eastward shift in cyclogenesis previously associated with historical El Nino events may instead be a consequence of co-occurring positive PMM[36]. In our ensemble the tropical VWS anomaly during the LIA is highly correlated (Fig. 5) with negative mean PMM during the LIA, in contrast to positive mean PMM during the MCA (Fig. 2f).

Proxy reconstructions of TC activity reveal that the transition from the end of the MCA through the early LIA was characterized by anomalously high TC activity in the deep tropical WNP. Although ENSO variability was lower over the last millennium relative to the instrumental period, transient increases in ENSO variability when centennial mean climate conditions promoted cyclogenesis and intensification near reconstruction sites could have generated this anomaly. The combination of periodic fluctuations in ENSO variability with secular changes to centennial mean climate conditions could explain spatial variability in TC activity across the west Pacific, whereas ascription to just one of these factors appears insufficient.

The GPI anomalies in our model ensemble are small relative to the anomalies in TC proxy reconstructions. Some of this discrepancy is likely explained by lower decadal-centennial variability in the Last Millennium experiment results relative to expectations based on paleoclimate proxy records[42-44]. For example, our model ensemble does produce anomalous meridional circulation during the LIA consistent with a contraction and southward shift of annual ITCZ movement (ED Fig. 8). However, the magnitude of the modeled anomaly is only about 1% of the last millennium mean, which falls short of multi-degree latitude shifts interpreted from proxy records[29,32]. Even a one-degree southward shift in the ITCZ following a strong volcanic eruption in the tropical northern hemisphere can increase GPI in the deep tropical North Pacific and decrease it poleward[45]. Thus, the model ensemble may have failed to capture additional LIA cyclogenesis variability associated with ITCZ shifts.

TC formation and intensification to typhoon strength in the Pacific near-equatorial region (0-5°N) are rare in the historical record, hindering analysis of trends and risk. Additionally, 21st century trends in TC genesis and track density for the Pacific deep tropics in the CMIP5 models are small, with low inter-model agreement on their direction[18,46]. CMIP5 GCMs may also not adequately resolve processes necessary for such perturbations to develop. Our reconstruction circumvents the limitations of historical records and GCMs and demonstrates that cyclogenesis in the Pacific deep tropics has similar centennial variability as TC landfalls captured in higher latitude reconstructions. Thus, TC climatology in the deep tropics is non-stationary, and lack of adequate historical sampling or inter-model agreement in projections does not necessarily indicate that TC genesis there has a muted response to climatic forcing.

The coincidence of major hydroclimate/regional atmospheric circulation shifts during the LIA with enhanced deep tropical cyclogenesis at Jaluit and in the SCS provides a basis for extrapolating TC climatological response to similar shifts projected for the 21st century. The PWC is projected to weaken and shift east[47,48], potentially reducing cyclogenesis in the SCS, but promoting it in the Central Pacific. Additionally, recent tropical expansion due to anthropogenic warming and natural variability[49] has been connected with reduced cyclogenesis in the deep tropics and enhanced cyclogenesis at higher latitudes[35]. Our analysis suggests that anthropogenic radiative forcing may cause trends in Pacific deep tropical cyclogenesis that mirror the MCA-LIA transition, with cyclogenesis decreasing in the western deep tropical Pacific.

## References

1. Peduzzi, P. et al. Global trends in tropical cyclone risk. *Nat. Clim. Change* **2**, 289-294 (2012).

2. Emanuel, K., DesAutels, C., Holloway, C., and Korty, R. Environmental controls of tropical cyclone intensity. *J. Atmos. Sci.* **61**, 843-857 (2004).

3. Gray, W.M. Global view of the origin of tropical disturbances and storms. *Mon. Weather Rev.* **96**, 669-700 (1968).

4. Wu, L., Wen, Z., Huang, R., and Wu, R. Possible linkage between the monsoon trough variability and the tropical cyclone activity over the western North Pacific. *Mon. Weather Rev.* **140**, 140-150 (2012).

5. Brandon, C.M., Woodruff, J.D., Lane, P., and Donnelly, J.P. Tropical cyclone wind speed constraints from resultant storm surge deposition: A 2500 year reconstruction of hurricane activity from St. Marks, FL. *Geochem. Geophy. Geosy.* **14**, 2993-3008 (2013).

6. van Hengstum, J.P. et al. The intertropical convergence zone modulates intense hurricane strikes on the western North Atlantic margin. *Sci. Rep.* **6**, 21728 (2016).

7. Gao, S., Zhi, L., Zhang, W., and Chen, Z. Strong modulation of the Pacific Meridional Mode on the occurrence of intense tropical cyclones over the western North Pacific. *J. Climate* **31**, 7739-7749 (2018).

8. Huang, S. and Oey, L.Y. Land-falling typhoons are controlled by the meridional oscillation of the Kuroshio Extension. *Clim. Dynam.* **52**, 2855-2867 (2018).

9. Woodruff, J.D., Kanamaru, K., Kundu, S., and Cook, T.L. Depositional evidence for the Kamikaze typhoons and links to changes in typhoon climatology. *Geology* **43**, 91-94 (2015).10. Liu, K., Shen, C., Louie, K. A 1,000-year history of typhoon landfalls in Guangdong, Southern China, reconstructed from Chinese historical documentary records. *Ann. Assoc. Am. Geogr.* **91**, 453-464 (2001).

11. Yu, K.F., Zhao, J.X., Shi, Q., and Meng, Q.S. Reconstruction of storm/tsunami records over the last 4000 years using transported coral blocks and lagoon sediments in the southern South China Sea. *Quatern. Int.* **195**, 128-137 (2009).

12. Donnelly, J.P. et al. Climate forcing of unprecedented intense-hurricane activity in the last 2000 years. *Earth's Future* **3**, 49-65 (2015).

13. van Hengstum, P.J. et al. Heightened hurricane activity on the Little Bahama Bank from 1350 to 1650 AD. *Cont. Shelf Res.* **86**, 103-115 (2014).

14. Lane, P., Donnelly, J.P., Woodruff, J.D., and Hawkes, A.D. A decadally-resolved paleohurricane record archived in the late Holocene sediments of a Florida sinkhole. *Mar. Geol.* **287**, 14-30 (2011).

15. Gischler, E., Shinn, E.A., Oschmann, W., Fiebig, J., and Buster, N.A. A 1500-year Holocene Caribbean climate archive from the Blue Hole, Lighthouse Reef, Belize. *J. Coastal Res.* **24**, 1495-1505 (2008).

16. Donnelly, J.P. et al. 700 yr sedimentary record of intense hurricane landfalls in southern New England. *GSA Bull.* **113**, 714-727 (2001).

17. Yan, Q., Wei, T., and Zhang, Z. Variations in large-scale tropical cyclone genesis factors over the western North Pacific in the PMIP3 last millennium simulations. *Clim. Dyn.* **48**, 957-970 (2016).

18. Zhang, L., Karnauskas, K.B., Donnelly, J.P., and Emanuel, K. Response of the North Pacific tropical cyclone climatology to global warming: Application of dynamical downscaling to CMIP5 Models. *J. Climate* **30**, 1233-1243 (2017).

19. Blumenstock, D.I. Typhoon effects at Jaluit Atoll in the Marshall Islands. *Nature* **182**, 1267-1269 (1958).

20. Toomey, M.R., Donnelly, J.P., Tierney, J.E. South Pacific hydrologic and cyclone variability during the last 3000 years. *Paleoceanography* **31**, 491-504 (2016).

21. Toomey, M.R., Donnelly, J.P., and Woodruff, J.D. Reconstructing mid-late Holocene cyclone variability in the Central Pacific using sedimentary records from Tahaa, French Polynesia. *Quaternary Sci. Rev.* **77**, 181-189 (2013).

22. Kench, P.S., McLean, R.F., Owen, S.D., Tuck, M., and Ford, M.R. Storm-deposited coral blocks: A mechanism of island genesis, Tutaga Island, Funafuti Atoll, Tuvalu. *Geology* **46**, 915-918 (2018).

23. Kim, H.M., Webster, P.J., and Curry, J.A. Modulation of North Pacific tropical cyclone activity by three phases of ENSO. *J. Climate* **24**, 1839-1849 (2011).

24. Patricola, C.M., Camargo, S.J., Klotzbach, P.J., Saravanan, R., and Chang, P. The influence of ENSO flavors on western North Pacific tropical cyclone activity. *J. Climate* **31**, 5395-5416 (2018).

25. Denniston, R.F. et al. Extreme rainfall activity in the Australian tropics reflects changes in the El Nino/Southern Oscillation over the last two millennia. *PNAS* **112**, 4576-4581 (2015).

26. Emile-Geay, J., Cobb, K.M., Mann, M.E., Wittenberg, A.T. Estimating central equatorial Pacific SST variability over the past millennium. Part II: Reconstructions and implications. *J. Climate* **26**, 2329-2352 (2013).

27. Liu, Y. et al. Recent enhancement of central Pacific El Nino variability relative to last eight centuries. *Nat. Commun.* **8**, 15386 (2017).

28. Emile-Geay, J. et al. Links between tropical Pacific seasonal, interannual and orbital variability during the Holocene. *Nat. Geosci.* **9**, 168-173 (2015).

29. Denniston, R.F. et al. Expansion and contraction of the Indo-Pacific tropical rain belt over the last three millennia. *Sci. Rep.* **6**, 34485 (2016).

30. Yan, H. et al. South China Sea hydrological changes and Pacific Walker Circulation variations over the last millennium. *Nat. Commun.* **2**, 293 (2011).

31. Yan, H. et al. Dynamics of the intertropical convergence zone over the western Pacific during the Little Ice Age. *Nat. Geosci.* **8**, 315-320. (2015).

32. Sachs, J.P. et al. Southward movement of the Pacific intertropical convergence zone AD 1400-1850. *Nat. Geosci.* **2**, 519-525 (2009).

33. Thompson, L.G. et al. Annually resolved ice core records of tropical climate variability over the past ~1800 years. *Science* **340**, 945-950 (2013).

34. Kossin, J.P., Emanuel, K.A., and Camargo, S.J. Past and projected changes in western north Pacific tropical cyclone exposure. *J. Climate* **29**, 5725-5739 (2016).

35. Sharmila, S. and Walsh, K.J.E. Recent poleward shift of tropical cyclone formation linked to Hadley cell expansion. *Nat. Clim. Change* **8**, 730-736 (2018).

36. Hong, C.C., Lee, M.Y., Hsu, H.H., Tseng, W.L. Distinct influences of the ENSO-like and PMM-like SST anomalies on the mean TC genesis location in the western North Pacific: The 2015 summer as an extreme example. *J. Climate* **31**, 3049-3059 (2018).

37. Emanuel, K., and Nolan, D. Tropical cyclone activity and global climate. In *Proceedings of the 26th Conference on Hurricanes and Tropical Meteorology* 240-241 (American Meteorological Society, 2004).

38. Emanuel, K. Tropical cyclone activity downscaled from NOAA-CIRES reanalysis, 1908-1958. *J. Adv. Model. Earth Sy.* **2**, 1-12 (2010).

39. Camargo, S.J., Emanuel, K.A., and Sobel, A.H. Use of a genesis potential index to diagnose ENSO effects on tropical cyclone genesis. *J. Climate* **20**, 4819-4834 (2007).

40. Chiang, J.C.H. and Vimont, D.J. Analogous Pacific and Atlantic meridional modes of tropical atmosphere-ocean variability. *J. Climate* **17**, 4143-4158 (2004).

41. Chang, P. et al. Pacific meridional mode and El Nino-Southern Oscillation. *Geophys. Res. Lett.* **34**, L16608 (2007).

42. PAGES Hydro2k Consortium. Comparing proxy and model estimates of hydroclimate variability and change over the Common Era. *Clim. Past* **13**, 1851-1900 (2017).

43. Ault, T.R., Deser, C., Newman, M., and Emile-Geay, J. Characterizing decadal to centennial variability in the equatorial Pacific during the last millennium. *Geophys. Res. Lett.* **40**, 3450-3456 (2013).

44. Zanchettin, D., Rubino, A., Matei, D., Bothe, O., and Jungclaus, J.H. Multidecadal-to-centennial SST variability in the MPI-ESM simulation ensemble for the last millennium. *Clim. Dyn.* **40**, 1301-1318 (2013).

45. Pausata, F.S.R. and Camargo, S.J. Tropical cyclone activity affected by volcanically-induced ITCZ shifts. *PNAS* **116**, 7732-7737 (2019).

46. Camargo, S.J. Global and regional aspects of tropical cyclone activity in the CMIP5 models. *J. Climate* **26**, 9880-9902 (2013).

47. Chung, E.S. et al. Reconciling opposing Walker circulation trends in observations and model projections. *Nat. Clim. Change* **9**, 405-412 (2019).

48. Vecchi, G.A. and Soden, B.J. Increased tropical Atlantic wind shear in model projections of global warming. *Geophys. Res. Lett.* **34**, L08702 (2007).

49. Staten, P.W. et al. Tropical widening: From global variations to regional impacts. *Bull. Amer. Meteor. Soc.* **101**, E897-E904 (2020).

50. Cobb, K.M. et al. Highly variable El Nino-Southern Oscillation throughout the Holocene. *Science* **339**, 67-70 (2013).

**Corresponding author**

Correspondence should be directed to James F. Bramante at e-mail address: James.F.Bramante@gmail.com

**Acknowledgements**

We thank student intern David Carter for extensive labwork on core LTD3. This work was supported by the Strategic Environmental Research and Development Program (SERDP RC-2336). C. U. acknowledges support from NSF under AGS-1602455. We acknowledge the WCRP's Working Group on Coupled Modelling, which is responsible for CMIP, and we thank the climate modeling groups for producing and making available their model output. CMIP5 model output was provided by the WHOI CMIP5 Community Storage Server, from their website at http://cmip5.whoi.edu/. Any use of trade, firm, or product names is for descriptive purposes only and does not imply endorsement by the U.S. Government.

**Author contributions**

J.B. performed labwork, model analysis, and wrote the initial draft. J.B., M.F., P.K., A.A., M.T., R.S., and J.D. performed the fieldwork and advised on sedimentology analysis and interpretation. K.K. and C.U. advised on model analysis and interpretation. All authors discussed the results, commented on the manuscript, and contributed revisions.

**Competing interests**

The authors declare no competing financial or non-financial interests.

**FIGURES**

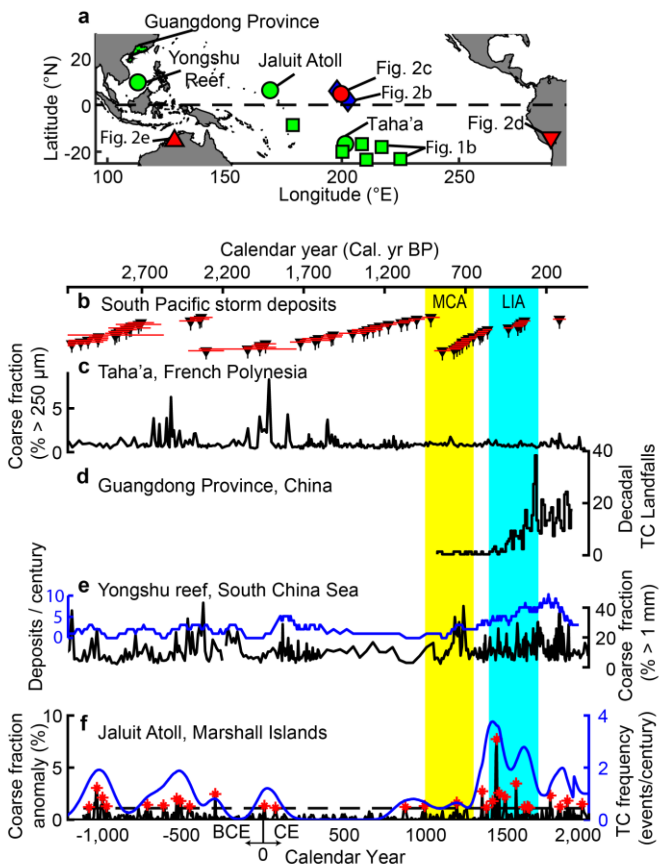


**Figure 1.** Western Pacific tropical cyclone reconstructions. a) the location of records in Figs. 1 and 2, symbol definitions can be found in ED Fig. 1; b) radiocarbon dates (+/- 1 standard deviation) from South Pacific storm-deposited boulders[21,22]; c) storm deposits in a back-barrier reef lagoon, Taha'a, French Polynesia[20]; d) TC landfalls in Guangdong Province and imperial Chinese historical records[10]; e) coarse fraction (black line) and centennial frequency (blue line) of large wave deposits at Yongshu Reef[11]; f) 250-2000 µm coarse fraction anomaly (black line) from Jaluit Atoll and centennial frequency (blue line) of identified storm deposits (red asterisks) (this study). Error in b), d) and e) is less than ±0.05%, too small for plotting. Uncertainty estimates were unavailable for c). MCA = Medieval Climate Anomaly. LIA = Little Ice Age.

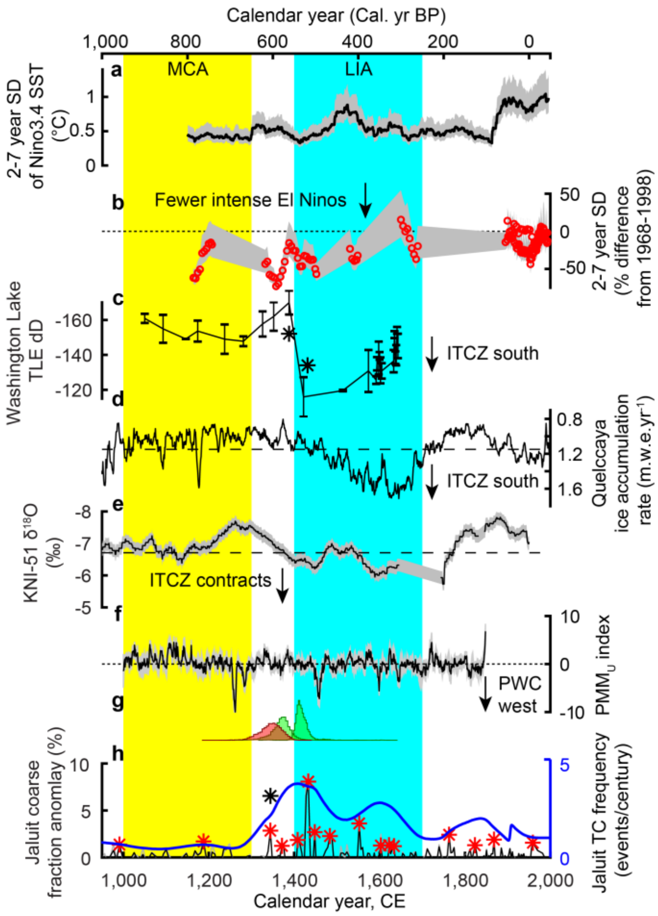


**Figure 2.** Comparison of our storm reconstruction with Pacific paleoclimate proxies. a) ENSO-band standard deviation (SD), calculated in a 31-year moving window, of a multi-proxy reconstruction of Nino3.4 region SST anomalies[26]; b) normalized ENSO-band SD of SSTs from coral $\delta^{18}$O proxies[28,50]; c) lipid $\delta$D proxy of precipitation from Washington Lake, Washington Island, Northern Line Islands[32]; d) ice accumulation rates in meters water equivalent (m.w.e.) in a core from the Quelccaya ice cap, Peru[33]; e) speleothem $\delta^{18}$O proxy of precipitation from cave KNI-51, northwestern Australia[29]; f) CMIP5 ensemble median (black line) +/- standard error (grey shading) of decadally-averaged PMM wind index anomaly (this study); g) comparison of age model histograms from samples indicated by black asterisks in c) and h); h) same as Fig. 1e. Dashed black lines indicate 1000-1850 CE means, dotted black lines indicate zero

values. Gray shading in a), b), and e) indicate 95% confidence intervals. Uncertainty estimates unavailable for d).

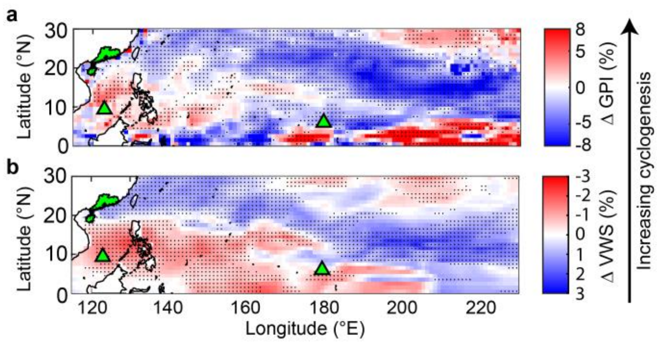


**Figure 3.** Change in tropical cyclogenesis potential from the Medieval Climate Anomaly (MCA, 1000-1300 CE) to the Little Ice Age (LIA, 1400-1700 CE). Ensemble median relative anomaly ($\Delta$ = (LIA - MCA) / MCA $\times$ 100%) of a) genesis potential index (GPI) and b) vertical wind shear (VWS). Anomalies for all GPI components are plotted in ED Fig. 5. Anomalies were calculated from northern hemisphere storm season (JASON) averages. Black stippling indicates five of seven models agree on change direction. Green symbols represent locations of storm reconstructions (ED Fig. 1).

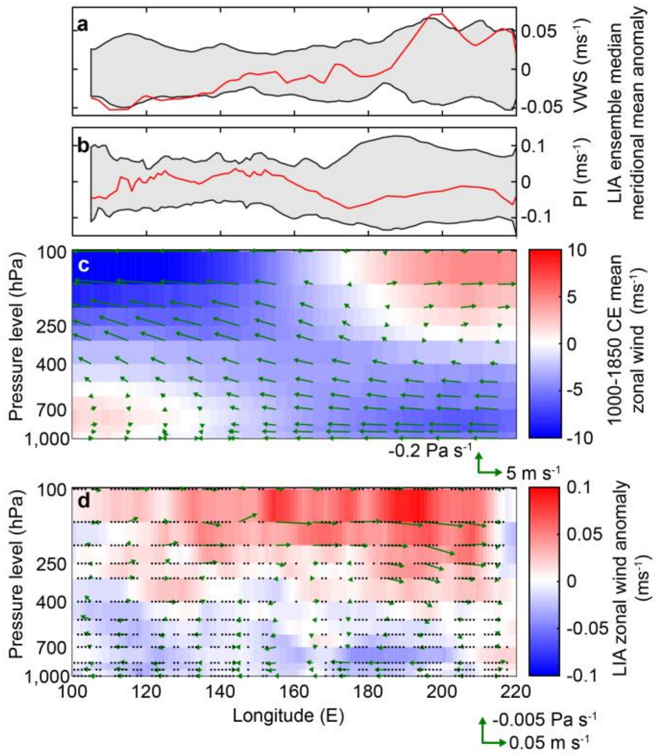


**Figure 4.** Relationship between vertical wind shear anomalies and the Pacific Walker Circulation. Ensemble median a) Vertical wind shear (VWS) anomaly (red line) and b) potential intensity (PI) anomaly (red line) during the LIA relative to 1000-1850 CE. c) Mean zonal wind (1000-1850 CE) (arrows, shading) and vertical pressure velocity (arrows). d) LIA anomaly of zonal wind (arrows, shading) and vertical pressure velocity (arrows). Gray shading in a,b) encompasses the 95% confidence interval of ensemble medians from all 300 year periods within 1000-1850 CE. Stippling in d) as in Fig. 3. All quantities are ensemble medians and meridional averages over 0°N-20°N.

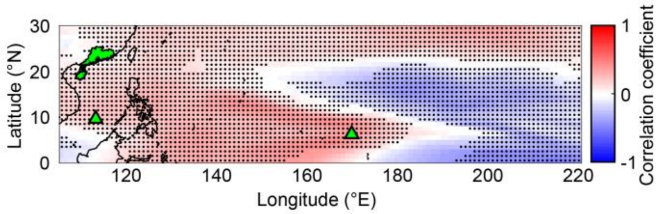


**Figure 5.** Ensemble median correlation between annual mean vertical wind shear and the Pacific Meridional Mode wind index in GCM ensemble results. Stippling indicates agreement on the direction of the correlation by at least five of seven models. Model-specific correlation maps can be found in ED Fig. 7.

## METHODS

### Study site and field methods

We developed a sediment proxy reconstruction of TC activity at Jaluit Atoll in the southern Marshall Islands. Jaluit is a mid-ocean atoll with a 250-1000 m wide intertidal reef flat encircling a shallow lagoon. The mildly stratified blue hole from which we extracted sediment cores LTD2 and LTD3 is located on the northwestern tip of Jaluit, where the atoll rim is widest (ED Fig. 1). The blue hole is flanked by three small, vegetated islands between which smooth channels connect it to the ocean-facing reef flat, which is covered in crustose coralline algae. The blue hole is backed by a deeper reef flat, 400 m-wide with actively growing coral.

The sediment cores were retrieved using a Rossfelder P-3 vibracoring system. For core LTD2, a separate surface drive of the upper 1-1.5 m of sediment was retrieved to preserve the sediment surface, because the primary drive over-penetrated. Coring sites were selected based on bathymetry and absence of hard substrate such as large coral heads. Bathymetry and seismic surveys were recorded using an Edgetech 3100 Chirp sub-bottom sonar system with a 4–24 kHz fish towed behind a small outboard-motor craft. Cores were sectioned in the field before transportation to the lab.

### Laboratory analysis

Cores were split and described in the lab (SI Core descriptions), then sampled at 1-cm intervals. Samples were wet-sieved at 63 µm and dry-sieved at 250 and 2000 µm to obtain dry weight-normalized grain size fractions at each sieve size.

We established age controls for each core with a series of accelerator mass spectrometer (AMS) radiocarbon dates (ED Table 1) and assumed core-top dates. Where available, we sampled terrestrial organic macrofossils for dating, but they were rare, especially below the first few meters. Most of our core dates were measured from detrital inorganic carbonate, and thus have reduced precision and greater uncertainty due to the marine reservoir effect. All radiocarbon dating was performed at the National Ocean Sciences Accelerator Mass Spectrometer (NOSAMS, Woods Hole, MA, USA) facility. Sediment at the top of each core was assumed deposited immediately prior to core extraction in November 2015. The top core section of the LTD2 primary drive did not capture the sediment-water interface, so the location of the core-top was inferred from the separate surface drive using a near-surface tie point. Using tie points this way assumes deposition rate in the vicinity of the core-top was equal between the primary and surface drive. For LTD2, we used the base of a large coarse event bed as a tie point (ED Fig. 2). The base of a large storm event bed common to all LTD2 and LTD3 drives was used as an additional tie point for LTD3 age control (Supplementary Methods).

The LTD3 age model (ED Fig. 2) was generated using the Bayesian age modeling software BACON[51], using the IntCal13 curve for terrestrial organic carbon dates[52], the Marine13 curve for inorganic carbon dates from detrital carbonate sediment grains[52], and Northern Hemisphere Zone 3 (ITCZ region) post-bomb curve for one post-bomb date[53]. BACON constructs an ensemble of accumulation histories through Markov Chain Monte Carlo iteration on provided dates and thus provides a distribution of likely ages for every centimeter of the core. Inorganic carbonate dates were corrected for a marine reservoir effect using $\Delta R = 41 \pm 42$ yr, determined for the past 2500 years from branching coral samples retrieved from Ebon Atoll, Republic of the Marshall Islands, 200 km southwest of the Jaluit blue hole[54].

**Event bed selection**

We used a simple statistical analysis of sediment grain size to identify event beds in our cores (ED Fig. 3). First, outliers were identified as samples of coarse fraction that exceeded 2 standard deviations above the mean coarse fraction, both statistics calculated within an 11-cm moving window, encompassing roughly 50 years according to the age model. Then the moving average was recalculated, but this time excluding outliers. Finally, event beds were identified as peaks in the moving average-subtracted coarse fraction anomaly that exceeded 1.5 standard deviations of coarse fraction, calculated for the entire core excluding outliers. Removing outliers from the analysis prevented particularly large event beds from masking the presence of smaller peaks nearby, and using the moving window removed the influence of decadal variability in the background coarse fraction signal. We found that increasing the window size, increasing the threshold coarse anomaly, and including outliers affected the absolute number of event beds identified, but did not change the qualitative patterns in event bed frequency in core LTD3 (ED Figs. 4, 5). For the statistical analysis, we used the coarse fraction with sieve diameter between 250 μm and 2 mm to account for anomalous transport characteristics of very coarse bioclastic sediment (Supplementary Methods).

We calculated centennial event frequency using a procedure that incorporates uncertainty in the age model. For every identified storm event bed, we randomly sampled 9000 ages from the Bayesian age model ensemble and from them constructed a probability distribution function (PDF) with annual resolution. We then summed the values of all PDFs within a 100-year moving window, resulting in a time series of continuous centennial event frequency estimates incorporating relative uncertainty and age model shape for each event (ED Fig. 3). We modeled centennial event frequency in the record as a Poisson process and estimated a record-wide mean (95% confidence interval) event frequency of $\lambda$ = 0.95 (0.64-1.36) events/century at Jaluit by counting all identified event beds and dividing by the length of time captured by the core. As an alternative measure of mean event frequency, we examined 25,500 TCs dynamically downscaled for NCEP reanalysis climatology for the years 1996-2010 (see Zhang et al., 2017[18] for details). TCs with sustained wind speeds > 64 m/s (super typhoon/Category 4-5) passed within 75 km of the blue hole with a modern frequency of $\lambda$ = 1.39 events/century.

Inactive intervals in the core were identified as periods of time with zero events whose duration exceeded the 95% confidence interval (3-388 years) of a gamma distribution governing the time intervals between single events, with occurrence rate defined by the proxy Poisson process above. Active intervals are more difficult to define statistically, as different numbers of events occurring over different interval lengths can have the same probability of random occurrence. Thus, active intervals were first identified as those intervals in the frequency time series where the event frequency exceeded the 95% confidence interval of the Poisson distribution mean frequency for at least one century (ED Figs. 4, 5). The probability that each active interval was generated randomly (unforced) was then estimated using the cumulative distribution function of a gamma distribution defined by the proxy Poisson process above and the number of events contributing to the active interval, evaluated for the time interval between the first and last event. For example, 10 events make up the active interval roughly concurrent with the LIA, and the first and last occur at 1345 and 1634 CE, respectively. The probability that this interval was the random result of a Poisson process is $p < 0.001$ for $\lambda = 0.95$ events/century and $p = 0.008$ for the higher $\lambda = 1.39$ events/century. Under the simplifying assumption that our 3609-year record represents 3609/289=12.5 independent draws from this gamma distribution, the chances that the LIA peak would be randomly generated in any similar-length record would be 1.2% for $\lambda = 0.95$ events/century and 9.6% for $\lambda = 1.39$ events/century.

**Best track analysis**

To illustrate modern TC genesis and tracks in the vicinity of our reconstruction site under modern climate conditions, we calculated simple statistics on 6-hourly best track data from IBTrACS-WMO, v03r10[55] for western Pacific and eastern Pacific basins encompassing Jan. 1848 – Jun. 2017.

**Climate model analysis**

We used the results from seven general circulation models (GCMs) to explore possible drivers of anomalous TC climatology during the Little Ice Age (LIA). We used every model involved in the fifth iteration of the Coupled Model Intercomparison Project (CMIP5) that provided results for the Last Millennium experiment (ED Table 2), except for the Model for Interdisciplinary Research on Climate Earth System Model (MIROC-ESM), which was excluded because of its long-term drift[56]. Removal of FGOALS-g1 from the ensemble, leaving only one FGOALS member, did not qualitatively alter the results, but did reduce inter-model agreement some. We used monthly mean values for all of our analyses.

We quantified TC genesis potential using a genesis potential index (GPI)[37,38]:

$$GPI = |\eta|^{3}\, \chi^{-4/3}\, \mathrm{MAX}(PI - 35\ \mathrm{ms}^{-1}, 0)^{2}\, (25\ \mathrm{ms}^{-1} + VWS)^{-4},$$

where $\eta$ is absolute vorticity at 850 hPa; $\chi$ is a measure of the moist entropy deficit of the middle troposphere and represents an entropy gradient barrier to cyclone intensification[57]; *PI* is potential intensity, an estimate of maximum achievable wind speeds as a function of convectively available potential energy[58]; and *VWS* is absolute wind shear between 250 hPa and 850 hPa. As can be inferred from the sign of the exponent applied to each variable, vorticity and potential intensity tend to promote TC formation and intensification, respectively, while the moist entropy deficit and wind shear tend to depress or interrupt formation and intensification, respectively.

Here we define vertical wind shear (VWS) as the difference between winds at 850 hPa and at 250 hPa to be consistent with previous research defining and applying GPI[18,38,59]. However, some previous work has instead used the difference in winds at 850 hPa and 200 hPa to define VWS and alternative TC genesis indexes. We investigated vertical profiles of mean winds in the western North Pacific and found that the variability (with and without seasonality included) of 200 hPa and 250 hPa winds is very highly correlated in the Last Millennium experiment model results. Additionally, recalculating GPI and VWS using 200 hPa winds did not qualitatively affect our results. Additionally, neglecting components of GPI that have historically not correlated strongly with temporal trends in cyclogenesis did not affect our results qualitatively (see Supplementary Discussion).

GPI was calculated using monthly mean climate model output. In reality, TCs would be expected to respond to variability in the input variables over daily or sub-daily timescales, and that variability is lost when calculating e.g. vertical shear from monthly mean wind velocity instead of taking the monthly mean of daily VWS.  Previous research has found that trends in VWS change little whether calculated from daily-mean or monthly-mean wind velocity and then averaged over longer climatological timescales[48,60]. Here we assume that calculating GPI using higher temporal resolution model output would not alter our results qualitatively.

We calculated GPI and all of its components at each model's native spatial resolution before interpolating linearly to a common 1° x 1° grid. Relative anomalies in each index between the LIA (1400-1700 CE) and the MCA (1000-1300 CE) were calculated according to (LIA - MCA) / MCA x 100% for each model.  Multi-model ensemble averaging was performed using the median statistic as the last step in any analysis where it is presented (e.g. percent change between the MCA and LIA was calculated for each model separately and then the median taken for a multi-model ensemble value and displayed in Fig. 3). For all comparisons, time averages include only values the primary storm season, i.e. July-November (JASON) in the North Pacific.

To determine the magnitude of VWS (potential intensity) anomalies during the LIA relative to variability throughout the last millennium, we conducted a bootstrap analysis in which we calculated the ensemble median, meridional mean shear (potential intensity) anomaly, relative to the last millennium mean, for every 300-year period within the last millennium experiment results. From these populations we calculated the 95% confidence intervals of the anomalies at each latitude.

The Pacific Meridional Mode (PMM) indexes were calculated from SST and meridional and zonal surface wind fields for 20°S-30°N, 150-265°E. First, the influence of ENSO variability on the fields was removed by subtracting a linear least squares fit between the fields and the Cold Tongue Index, as in Chiang and Vimont[40]. Maximum Covariance Analysis was then applied to the cross-covariance matrix between SST and both wind fields (with land cells masked out). The PMM SST and wind indexes were identified with the second mode for the 1000-1850 CE period. We measured correspondence between mean annual storm season PMM and VWS using Spearman rank correlation for the years 1000-1850 CE. Statistical significance was calculated with a two-tail Student t-test after taking multiple testing into account with application of the false discovery rate procedure and setting q = 2.5%[61].

**Data Availability**

Grain size data, median ages by depth, centennial event frequency, and the dated material for core LTD3 are available on the National Oceanic and Atmospheric Administration National Centers for Environmental Information (NCEI) Paleoclimatology database <https://www.ncdc.noaa.gov/paleo/study/31132>, but can also be found on the Woods Hole Open Access Server (WHOAS), DOI:10.26025/1912/26159 <https://hdl.handle.net/1912/26159>. Much of the data from existing literature plotted in Figure 2 can be found on the NCEI paleoclimatology database (https://www.ncdc.noaa.gov/paleo-search/), using the following data set ids: Fig. 2a [noaa-recon-13684], Fig. 2b [noaa-coral-13672], Fig. 2c [noaa-lake-29432], Fig. 2d [noaa-icecore-14174], Fig. 2e [noaa-cave-20530]. Data for Fig. 1b and Fig. 1c are available as tables at DOI:

10.1016/j.quascirev.2013.07.019 [21] and supplementary information at DOI: 10.1002/2015PA002870 [20], respectively.

## Code Availability

The MATLAB code used to analyze the GCM output and the code and data used to plot figures are available on the Woods Hole Open Access Server (WHOAS), DOI:10.26025/1912/26159 <https://hdl.handle.net/1912/26159>.

## Methods References

51. Blauuw, M. and Christen, J.A. Flexible paleoclimate age-depth models using an autoregressive gamma process. *Bayesian Anal.* **6**, 457-474 (2011).

52. Reimer et al. IntCal13 and Marine13 radiocarbon age calibration curves 0-50,000 years cal BP. *Radiocarbon* **55**, 1869-1887 (2013).

53. Hua, Q., Barbetti, M., and Rakowski, A.Z. Atmospheric radiocarbon for the period 1950-2010. *Radiocarbon* **55**, 2059-2072 (2013).

54. Weisler et al. Marine reservoir correction for the southern Marshall Islands for the past 2500 years. *Radiocarbon* **60**, 333-348 (2018).

55. Knapp, K. R., Kruk, M. C., Levinson, D. H., Diamond, H. J. & Neumann, C. J. The International Best Track Archive for Climate Stewardship (IBTrACS) unifying tropical cyclone data. *Bull. Am. Meteorol. Soc.* **91**, 363–376 (2010)

56. Sueyoshi et al. Set-up of the PMIP3 paleoclimate experiments conducted using an Earth system model, MIROC-ESM. *Geosci. Model Dev.* **6**, 819-836 (2013).

57. Emanuel, K.A., Sundararajan, R., and Williams, J. Hurricanes and global warming: Results from downscaling IPCC AR4 simulations. *BAMS* **89**, 347-367 (2008).

58. Bister, M. and Emanuel, K.A. Dissipative heating and hurricane intensity. *Meteorol. Atmos. Phys.* **65**, 233-240 (1998).

59. Emanuel, K.A. Downscaling CMIP5 climate models shows increased tropical cyclone activity over the 21st century. *PNAS* **110**, 12219-12224 (2013).

60. Korty, R.L., Camargo, S.J., and Galewsky, J. Tropical cyclone genesis factors in simulations of the Last Glacial Maximum. *J. Climate* **25**, 4348-4365 (2012).

61. Hu, J., Emile-Geay, J., and Partin, J. Correlation-based interpretations of paleoclimate data – where statistics meet past climates. *Earth Planet. Sc. Lett.* **459**, 362-371 (2017).

## EXTENDED DATA

ED Table 1. Sediment core radiocarbon dates

| Core/ Drive | Sample Name | Accession # | Sample contents | Drive depth (cm) | $^{14}$C age (yr) | $^{14}$C error (yr) |
|---|---|---|---|---|---|---|
| LTD2/D2 | LTD2_D2_1:1_22-23cm | OS-133794 | Plant/wood | 23 | -5.645 | 0.25 |
| LTD2/D2 | LTD2_D2_1:1_105.5cm | OS-129304 | Plant/wood | 106 | 125 | 15 |
| LTD2/D1 | LTD2_D1_1:3_72cm[†] | OS-128853 | Coral | 72 | 550 | 20 |
| LTD2/D1 | LTD2_D1_2:3_64cm[†] | OS-128854 | Coral | 167 | 545 | 15 |
| LTD2/D1 | LTD2_D1_3:3_35-36cm | OS-127189 | Plant/wood | 259 | 350 | 15 |
| LTD2/D1 | LTD2_D1_3:3_84.5 | OS-127190 | Plant/wood | 308 | 330 | 15 |
| LTD3/D1 | LTD3_D1_1:5_45* | OS-127347 | Plant/wood | 45 | -465 | 16 |
| LTD3/D1 | LTD3_D1_1:5_48-49cm | OS-133795 | Plant/wood | 49 | 110 | 20 |
| LTD3/D1 | LTD3_D1_1:5_62cm[†] | OS-128851 | Mollusc | 62 | 515 | 15 |
| LTD3/D1 | LTD3_D1_2of5_25-26cm[†] | OS-151049 | Foraminifera | 126.5 | 735 | 15 |
| LTD3/D1 | LTD3_D1_2:5_52 | OS-127191 | Plant/wood | 152.5 | 560 | 15 |
| LTD3/D1 | LTD3_D1_2:5_59.5cm[†] | OS-129133 | Halimeda | 160 | 660 | 15 |
| LTD3/D1 | LTD3_D1_2of5_65-66cm[†] | OS-151050 | Foraminifera | 166.5 | 1040 | 15 |
| LTD3/D1 | LTD3-D1-3of5-3.5cm[††]* | OS-139903 | Mollusc | 223 | 740 | 160 |
| LTD3/D1 | LTD3_D1_3of5_25-26cm[†] | OS-151051 | Mollusc | 245 | 1,670 | 25 |
| LTD3/D1 | LTD3-D1-3of5-29cn[††] | OS-139904 | Mollusc | 248.5 | 1,460 | 160 |
| LTD3/D1 | LTD3_D1_3of5_52-53cm[†] | OS-151052 | Foraminifera | 272 | 1,930 | 25 |
| LTD3/D1 | LTD3-D1-3of5-113.5cm[††] | OS-139901 | Mollusc | 333 | 1,980 | 160 |
| LTD3/D1 | LTD3_D1_4of5_20-21cm[†] | OS-151053 | Foraminifera | 359.5 | 2,330 | 25 |
| LTD3/D1 | LTD3_D1_4of5_36-37cm | OS-149473 | Plant/wood | 375.5 | 2,110 | 20 |
| LTD3/D1 | LTD3_D1_4_41[††] | OS-125137 | Mollusc | 379.5 | 2,260 | 80 |
| LTD3/D1 | LTD3_D1_4of5_60-61cm[†] | OS-151054 | Foraminifera | 399.5 | 2,720 | 25 |
| LTD3/D1 | LTD3_D1_4_75p5[††] | OS-125138 | Mollusc | 414 | 2,350 | 80 |
| LTD3/D1 | LTD3_D1_4of5_99-100cm[†] | OS-151055 | Foraminifera | 438.5 | 2,700 | 30 |
| LTD3/D1 | LTD3_D1_5of5_12-13cm[†] | OS-151056 | Foraminifera | 481.5 | 2,890 | 20 |
| LTD3/D1 | LTD3_D1_5of5_36cm* | OS-141714 | Plant/wood | 496 | 390 | 20 |
| LTD3/D1 | LTD3_D1_5_38[††] | OS-125134 | Mollusc | 498.5 | 2,890 | 90 |
| LTD3/D1 | LTD3_D1_5of5_46.5cm* | OS-149409 | Plant/wood | 507 | 60 | 100 |
| LTD3/D1 | LTD3_D1_5of5_52-53cm[†] | OS-151057 | Foraminifera | 513 | 2,930 | 20 |
| LTD3/D1 | LTD3_D1_5_53p5[††] | OS-125136 | Mollusc | 514 | 2,710 | 90 |
| LTD3/D1 | LTD3_D1_5_75p5[††] | OS-125135 | Mollusc | 536 | 3,210 | 85 |

[†] Indicates inorganic carbonate sample processed with hydrolysis and conventional AMS.

[††] Indicates inorganic carbonate sample processed with gas ion source. All samples were processed at NOSAMS.

* Indicates outliers excluded from the age model (SI Core descriptions).

ED Table 2. Summary of CMIP5 models from which monthly mean data were used in the last millennium analysis

| Institute | Model | Country | LM Years CE | Atmospheric resolution Latitude (°) | Atmospheric resolution Longitude (°) |
|---|---|---|---|---|---|
| BCC | BCC-CSM1.1 | China | 850-2000 | 2.81 | 2.81 |
| NASA | GISS-E2-R | USA | 850-1850 | 2.00 | 2.50 |
| IPSL | IPSL-CM5A-LR | France | 850-1850 | 1.89 | 3.75 |
| LASG-IAP | FGOALS-g1 | China | 1000-2000 | 4.00 | 5.00 |
| LASG-IAP | FGOALS-s2 | China | 850-1850 | 1.71 | 2.81 |
| MPI-M | MPI-ESM-P | Germany | 850-1850 | 1.84 | 1.84 |
| NCAR | CCSM4 | USA | 850-1850 | 0.94 | 1.25 |

LM = Last Millennium experiment

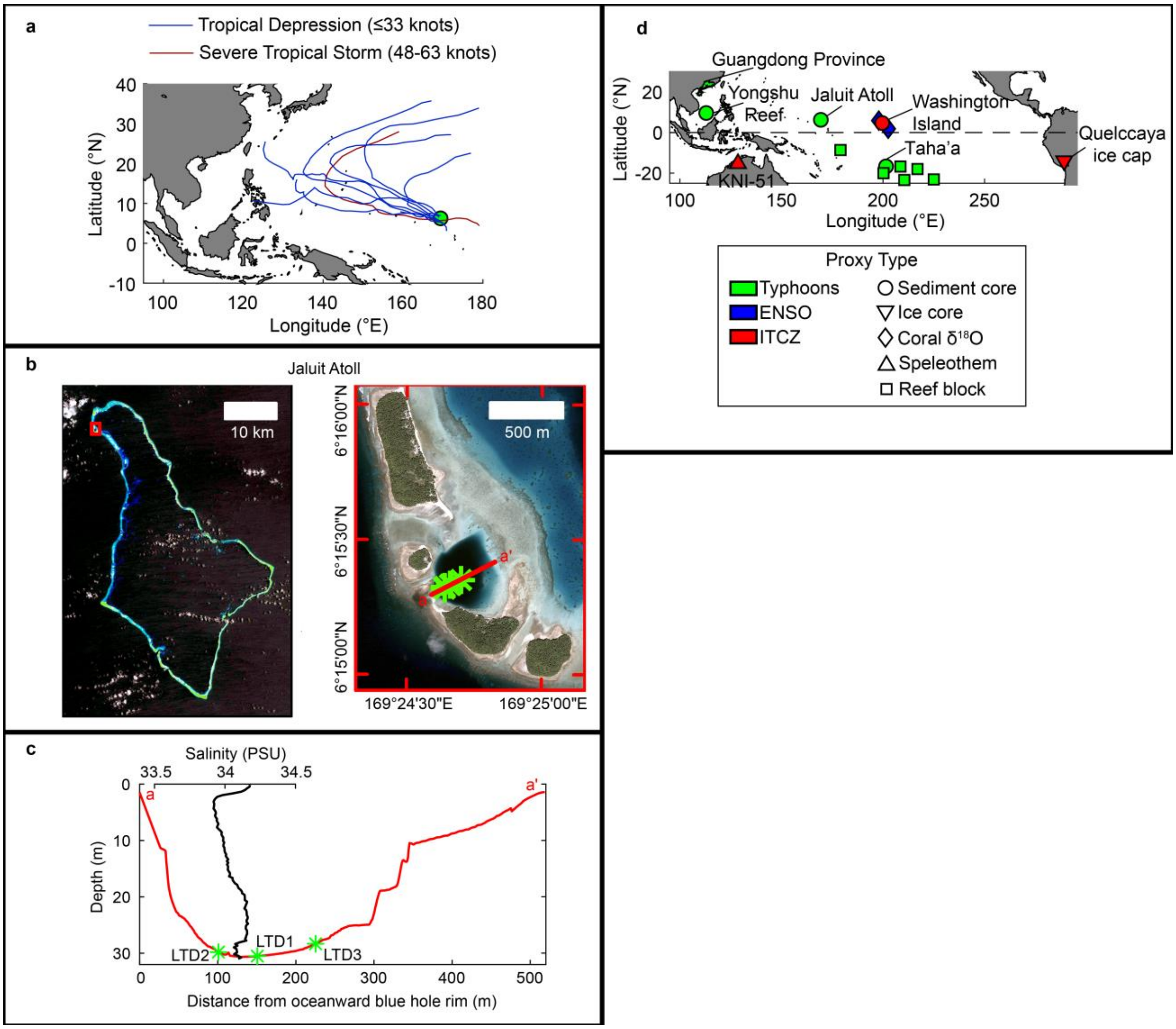


ED Figure 1. Maps of the reconstruction site: a) Map of the tropical western Pacific, with the storm tracks of every tropical cyclone in the IBTrACs dataset to pass within 100 km of Jaluit Atoll; b) map of the site showing location of cores as green asterisks; c) bathymetric profile of the basin from which the sediment cores were extracted, with a salinity profile; d) map of the tropical Pacific with locations of the reconstructions referenced in this study.

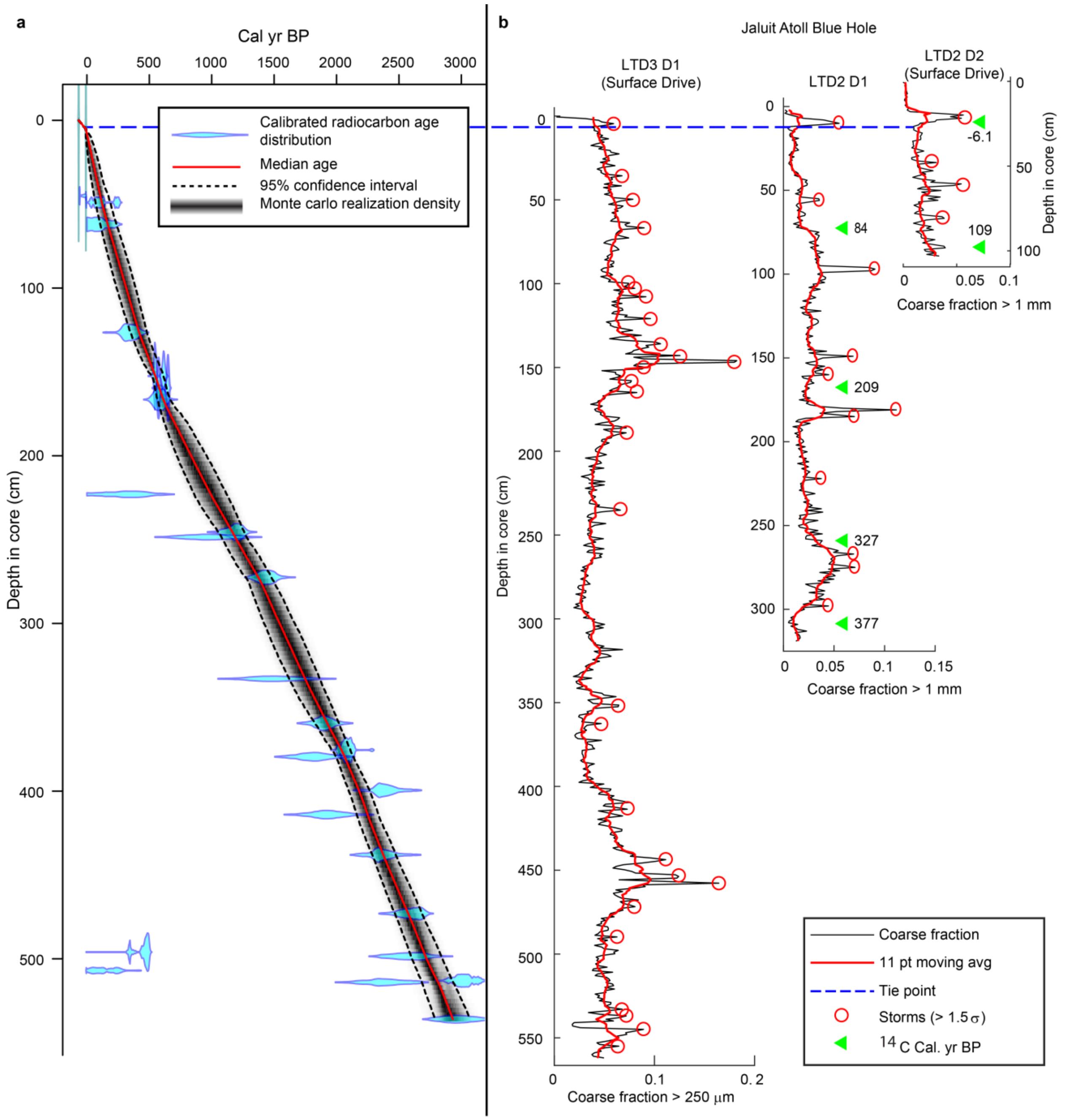


ED Figure 2. Profiles of sediment cores collected from the Jaluit Atoll blue hole. a) BACON age model for LTD3 and b) coarse fraction profiles of LTD2 and LTD3. BACON-calibrated radiocarbon dates are displayed as green triangles. A tie point used in the age models and to establish core top depth by comparing drives are indicated with a blue dashed line. Storm beds were identified as those samples that exceeded 1.5 standard deviations above an 11-cm moving average, where both statistics were calculated while ignoring >2 standard deviation outliers.

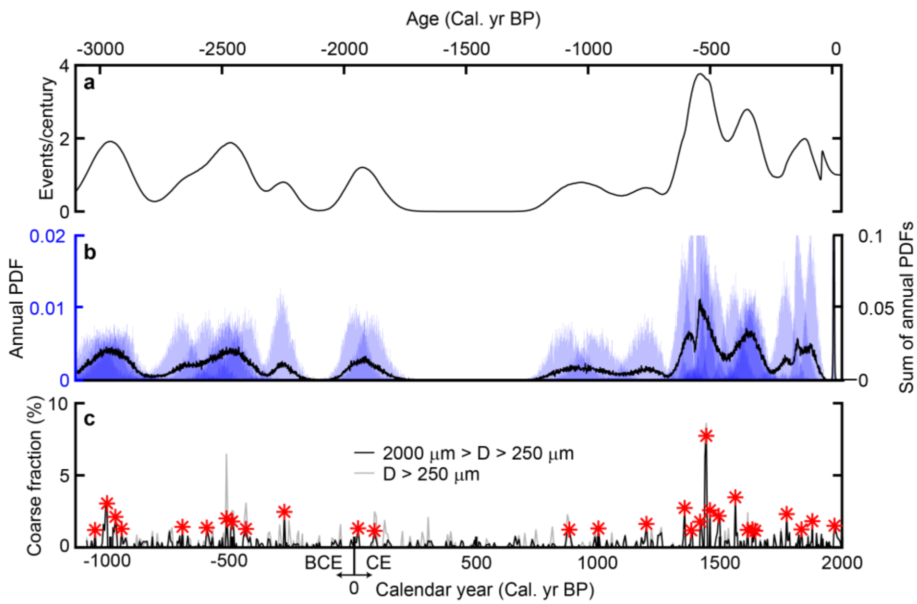


ED Figure 3. Illustration of the method used to calculate centennial event frequency from coarse fraction. c) Coarse fraction anomaly is used to identify event deposits as in Methods. b) The annually-binned probability distribution function (PDF, blue shading) of each event deposit is extracted from the age model and summed for each year (black line). a) The sum of annual PDFs is summed over a 100-year moving window to construct a time series of centennial event frequency incorporating age model uncertainty.

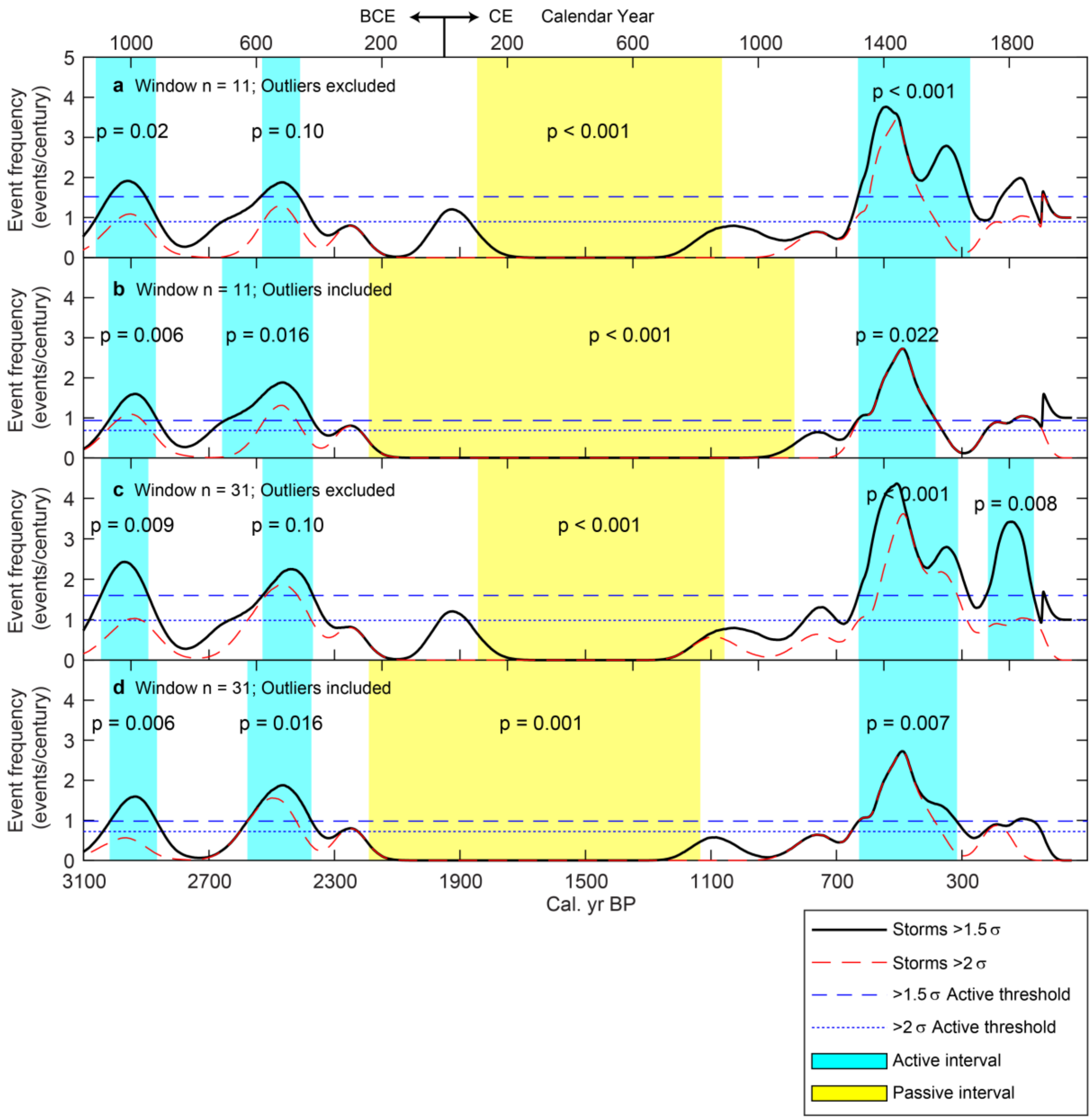


ED Figure 4. Sensitivity analysis of the procedure used to identify event beds in Jaluit Atoll core, LTD3 grain size data, using the 250-2000 μm coarse fraction. Coarse fraction variance over the entire core was calculated a) with a moving-average window-size of 11 cm and exclusion of outliers, b) with a moving average window size of 11 cm and inclusion of outliers, c) with a moving average window size of 31 cm and exclusion of outliers, and d) with a moving average window size of 31 cm and inclusion of outliers. For each of these four cases, event beds were flagged with 1.5 standard deviation and 2 standard deviation cutoffs. The active interval thresholds for each of these cutoffs represents the 97.5 percentile frequency for a Poisson distribution with the core's mean event frequency. Active intervals were identified as intervals lasting at least a century in which those thresholds were exceeded. Passive intervals were identified as intervals with zero events that were less than 2.5% likely to occur according to a gamma distribution. P-values are the cumulative frequency distribution values for a gamma distribution defined by a Poisson process defined by the cores centennial event frequency and the number of events contained in an active or passive interval, evaluated for the length of time between the first and last event in that interval.

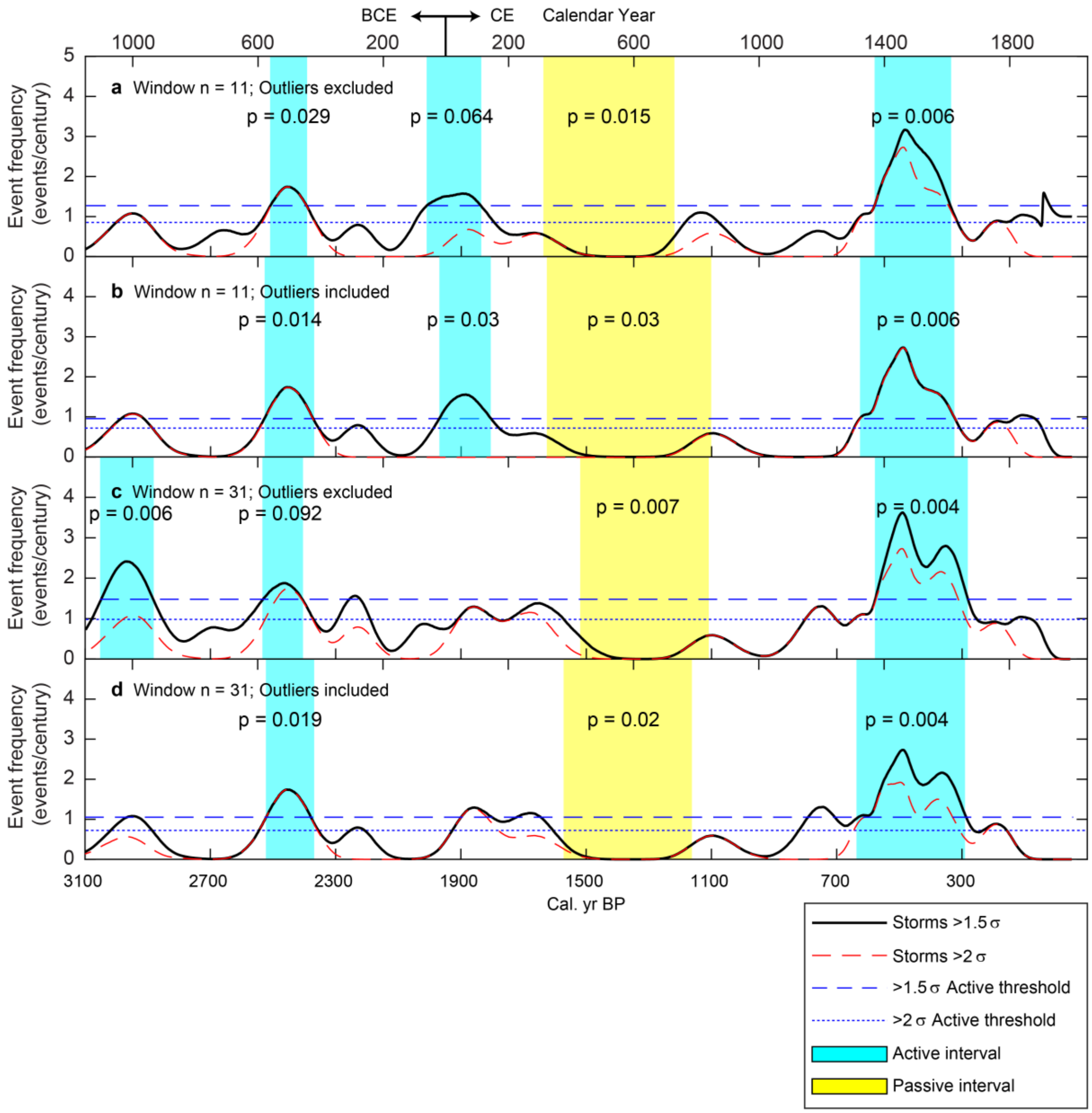


647

648 ED Figure 5. Same as Extended Data Fig. 4, but using the >250 μm coarse fraction.

649

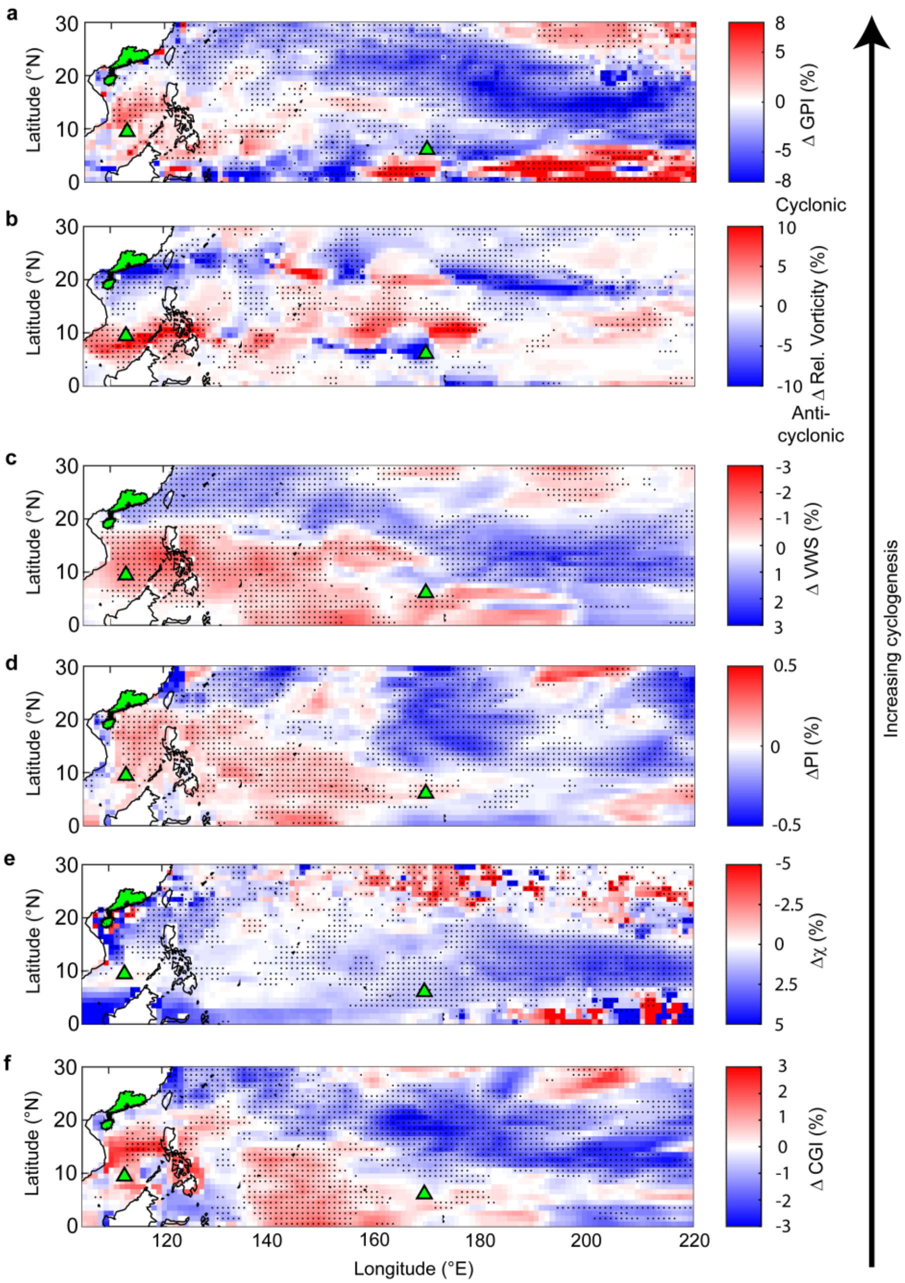


ED Figure 6. Ensemble median relative anomaly in tropical cyclone genesis indexes during the LIA (1400-1700 CE). Relative anomaly was calculated as $\Delta$ = (LIA - MCA) / MCA $\times$ 100%. The a) Genesis Potential Index[41] is calculated from four variables: b) low level vorticity, $\eta$ ($s^{-1}$), c) vertical wind shear ($ms^{-1}$), d) potential intensity ($ms^{-1}$), and e) the mid-troposphere saturation deficit, $\chi$ (dimensionless)[57]. The color palettes are aligned so red always indicates increasing cyclogenesis potential. The sign of relative vorticity in the southern hemisphere in b) was reversed so positive change indicates more cyclonic vorticity. Percent change values were calculated from storm season averages for the two time periods. In the northern hemisphere, the WNP storm season (JASON) was used. No data is shown for 1°S-1°N to indicate the different months used for averaging in each hemisphere. Black stippling indicates grid cells in which at least five of seven models agreed on the direction of change. The green symbols represent the locations of storm reconstructions (Extended Data Fig. 1).

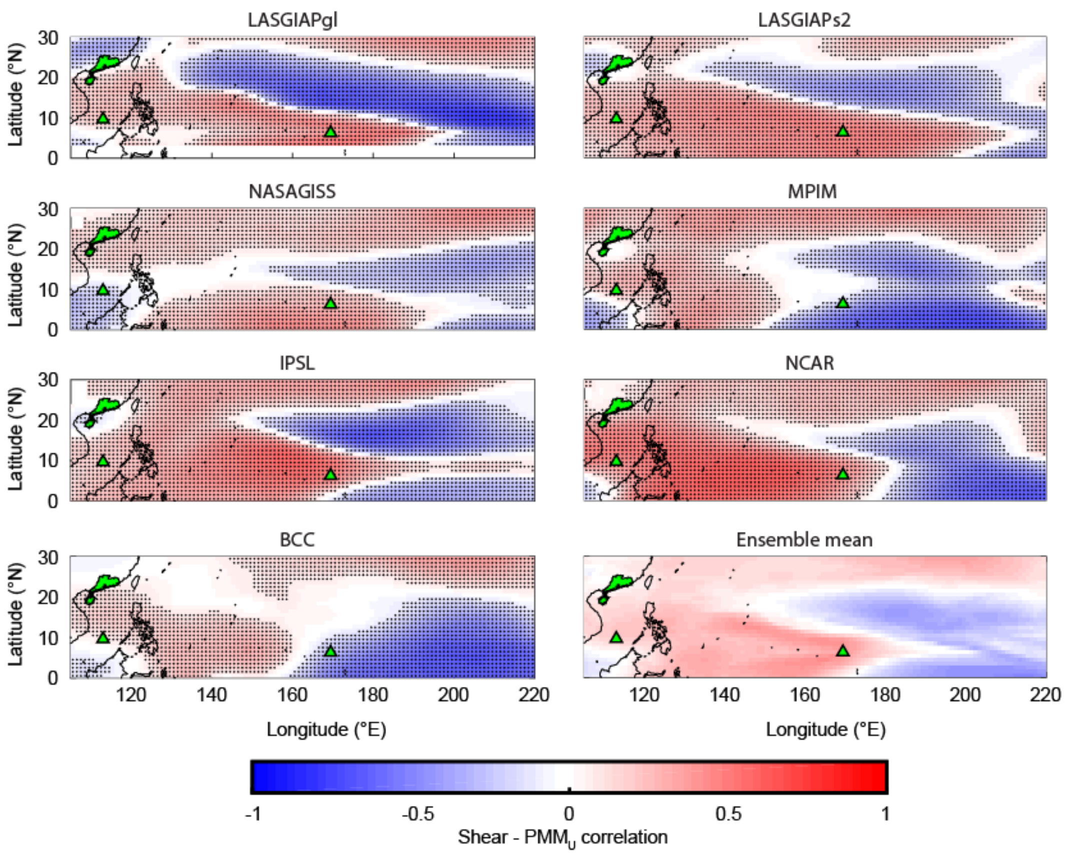


ED Figure 7. Spearman rank correlation between mean storm season vertical wind shear and Pacific Meridional Mode for each of the CMIP5 models. Correlation coefficients were calculated for Last Millennium experiment results for the period 1000-1850 CE. Black stippling indicates statistical significance as determined by a two-tailed Student t-test after taking into account multiple hypothesis testing using the false discovery rate procedure and setting q = 2.5%[61].

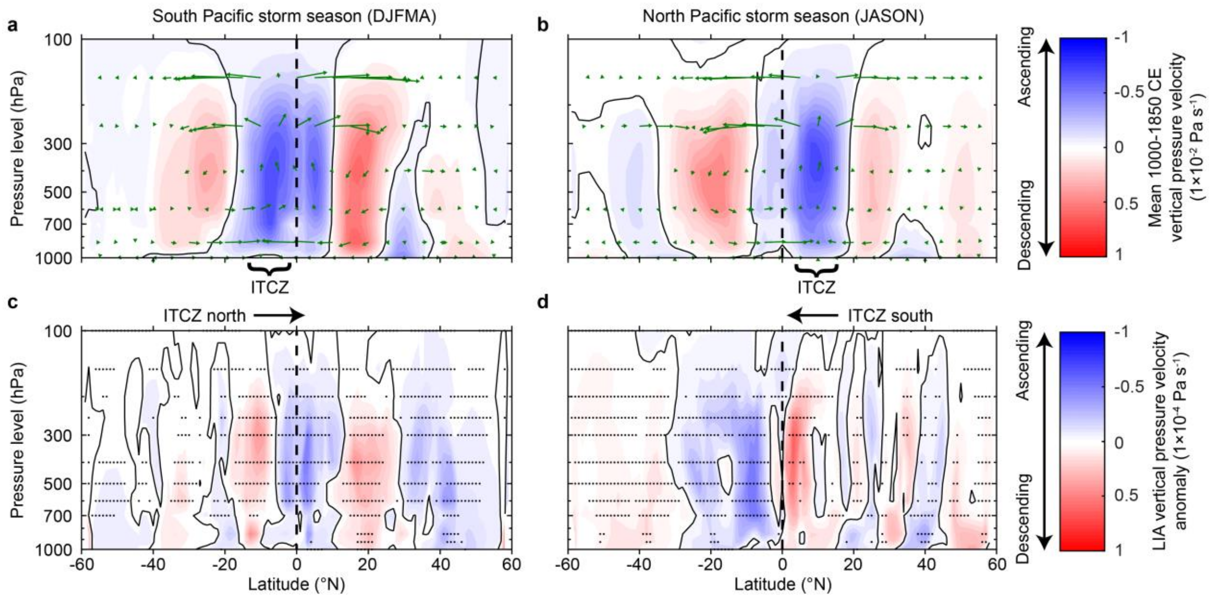


ED Figure 8. Hadley circulation anomalies during the Little Ice Age (1400-1700 CE). Zonal (100-180°E) mean vertical pressure velocity associated with meridional overturning circulation (shading, vectors) and non-divergent meridional wind velocity (vectors) a,b) averaged over 1000-1850 CE and c,d) the LIA (1400-1700 CE) anomaly relative to 1000-1850 CE. The dashed vertical lines indicate the equator. Negative (positive) vertical pressure velocity values indicate ascending (descending) motion. Black stippling in c,d) indicates pressure/latitude coordinates where at least 5 of the 7 models agreed on the direction of change.

## SUPPORTING INFORMATION

### Supplementary Methods

### Core descriptions

We retrieved primary (318 cm long) and surface (127 cm) drives for core LTD2 from 30 m depth at the oceanward end of the Jaluit Atoll blue hole (ED Fig. 1c). The surface of the core is characterized by a 15 cm layer of very fine to fine sand overlying a 10 cm-thick event bed of coarse sand and shell hash. Below this first event bed the core is characterized by visually uniform medium-coarse sand down to 296 cm, below which the sediment grades to fine sand. The core is visibly interspersed by large shell fragments and shell hash.

Core LTD3 was retrieved as a single, 561 cm-long drive from 28 m depth at the lagoonward end of the main blue hole basin. The surface of the core is characterized by a thin layer of silt that rapidly grades to fine to medium sand in the first few centimeters. The rest of the core is characterized by visually uniform, very fine to fine sand interspersed with shell fragments.

The sediment in our cores consists nearly entirely of detrital carbonate shell and skeletal material from foraminifera, coral, coralline algae, *Halimeda* green algae, echinoderms, and mollusks. Loss-on-ignition analysis of the organic carbon content was conducted at 10 cm intervals down the first 120 cm of LTD2 and 250 cm of LTD3. Organic carbon made up a uniform 4.5±0.1% (median ± standard deviation) of the sediment by dry weight in LTD2 and 4.3±0.1% in LTD3.

We submitted 25 samples for radiocarbon dating at NOSAMS. These included 6 organic carbon samples of root or bark material and 19 inorganic carbonate samples (8 foraminifera samples, 10 mollusc shell samples, and 1 *Halimeda* calcareous algae plate sample). Following previous studies demonstrating the presence of post-bomb radiocarbon in living *Halimeda*[62,63], which implies the absence or reduction of a marine reservoir effect for these shallow algae, we did not apply a marine reservoir effect for our 1 *Halimeda* sample. All but one of the inorganic carbonate samples returned calibrated ages implying a nearly constant sedimentation rate of c. 1.8 mm $y^{-1}$. However, three of the organic carbon samples returned anomalously young ages. We speculate that the anomalously young samples may have been dragged from a shallower depth during coring or core splitting. An alternative hypothesis, that the three young organic dates and one outlier inorganic carbon date define the sedimentation rate of the core, would imply that all of the inorganic carbonate material is reworked older material. The presence of older, reworked material is common in carbonate environments, but is generally apparent as a wide distribution of inorganic carbonate dates at many depths, with no obvious trend in mean age with depth (e.g. Chen et al.[64]). In contrast, our inorganic carbonate dates lie close to a line of nearly constant slope, which would be improbable if they were reworked material.

**Accounting for irregularly-shaped bioclastic sediment**

In this study, we use coarse deposits as a proxy for sediment transport induced by anomalously strong currents. In our implicit model, sediment is entrained over the surrounding shallow reef environment and transported across the blue hole basin, where some portion settles out of surface currents and is deposited in the blue hole. Assuming that grain size positively correlates with settling velocity, the strength of surface currents determines the maximum grain size mobilized and the distance sediment is transported across the blue hole before settling out of the surface currents. With slow, fair weather currents, mainly fine-grained sand and silt are deposited, while fast, storm-driven currents can mobilize and deposit thick layers of coarse sand. Using grain size as a proxy for anomalous mobilization and transport assumes that settling velocity strongly and monotonically increases with grain size. A very strong relationship between grain diameter and settling velocity exists for spherical and near-spherical sediment grains[65], but coarse biogenic carbonate sediment, like that produced in shallow reef environments, have irregular shapes and can have significant effective porosity, resulting in mobilization thresholds and settling velocities lower than would be predicted from their size[66-68]. In particular, above a characteristic grain diameter of about 2 mm, the settling velocity (and inferred mobilization threshold) of some bioclastic sediment plateaus[67,68]. If that sediment made up a substantial portion of the coarse fraction in a deposit, inferences about the strength of the current that mobilized and transported it before deposition could be invalidated.

Due to the deviation in the relationship between grain size and settling velocity for some bioclastic sediment, we identified event layers in core LTD3 using the sediment fraction with sieve diameter 250-2000 μm (herein the "corrected fraction"). We found that using the corrected fraction reduced the size of some apparent coarse layer peaks, especially below 3 m depth in the core (Fig. 1e). In a few instances apparent coarse peaks in the > 250 μm fraction were absent in the corrected fraction. For at least two of those peaks a solitary, intact, anomalously large gastropod shell generated most of the uncorrected coarse fraction peak, justifying the use of the corrected fraction here. However, we found that trends in event frequency were relatively invariant to the coarse fraction used for event identification (ED Figs. 4 and 5). In both coarse fractions there is an LIA active interval in event frequency preceded by a long, relatively quiescent interval. With the corrected fraction, the LIA active interval has a longer duration and peaks earlier (ED Fig. 4). However, both coarse fractions identify the same coarse deposit initiating the active interval.

## Supplementary Discussion

### TC proxy justification

The storms recorded in the Jaluit Atoll sediment cores were likely typhoon strength and higher (>64 kt sustained wind velocity). A post-bomb date taken from the most recent event bed in LTD2 indicates the event bed, present in all LTD cores, was likely deposited by severe typhoon Ophelia in 1958[19]. Age models developed for LTD2 and LTD3 suggest the second most recent event bed was deposited roughly 50 cal. yr BP, making it contemporaneous with an unnamed typhoon in 1905 known to have damaged islands and island villages across Jaluit Atoll[69]. The statistical process we used to identify storm events excluded lower magnitude peaks between these two events, implying our storm frequency reconstruction represents frequency of landfall or near misses by typhoons to the exclusion of less severe or more distant TCs. Additionally, the location of our site far from tsunamigenic earthquake activity along the Pacific Rim and the rarity of tsunamis relative to severe TCs in the WNP make it unlikely that tsunamis contaminated our storm record.

We argue that landfall frequency variability in our reconstructions is primarily a function of cyclogenesis conditions at near-equatorial latitudes to the south and southeast of our reconstruction site. Only 28 of 1703 TCs in the IBTrACS dataset that formed in or entered the WNP since 1848 formed east of 180°E. Only 8 of those formed below 10°N, and none crossed 180°E below 10°N, as WNP TCs very rarely move south, especially at low latitudes[70]. Thus, with modern climatology, TCs in our proxy records are unlikely to have formed far from the reconstruction site at 169.4°E. We assume the short travel distance means variability in our reconstruction is generated by variability in genesis conditions, and not post-genesis environmental factors.

Were genesis locations significantly further east sometime in the past, TCs would have traveled further and likely obtained higher intensities before making landfall at our site. Higher average landfall intensity would result in greater recorded landfall frequency, even if genesis frequency and intensity remained unchanged. Under these conditions, an independent change in environmental conditions that increased (decreased) post-genesis intensification would amplify (dampen) the effect of shifted genesis location. However, this post-genesis intensification still requires variability in genesis conditions, consistent with our assumption that the reconstructions reflect variability in cyclogenesis to the south and southeast of our site.

**Climate model analysis**

Although often calculated from monthly mean model and reanalysis data with spatial resolution lower than would be required to simulate realistic TCs explicitly, the Genesis Potential Index (GPI)[37,38] is a useful proxy for the frequency of TC genesis, especially at the ocean basin scale. At both global scale and for individual ocean basins, the seasonality of mean GPI correlates strongly with seasonal patterns in cyclogenesis[39]. Additionally, at the basin scale mean GPI replicates decadal variability in TC genesis over the instrumental period, although it does not perform as well when compared with inter-annual variability[71]. At the basin-level, GPI calculated from climate model results also closely correlates with predictions of cyclogenesis made by dynamic downscaling of GCM results[38]. Finally, the spatial distribution of storm season GPI within ocean basins replicates the distribution of historical genesis locations, and tends to be consistent across model and reanalysis products[72]. However, separate examination of each of the components of GPI has demonstrated that potential intensity and vertical wind shear are responsible for most of GPI's correlation with seasonal and inter-decadal variability in historical cyclogenesis.

Vorticity and the mid-tropospheric moist entropy deficit are necessary conditions for TC genesis, but historically do not contribute skill to predictions of temporal variability in TC genesis. In particular, monthly-mean absolute vorticity is a proxy for the prevalence of atmospheric disturbances that can act as a seed for TC convection[60], but marginal increases in absolute vorticity above some relatively low threshold don't appear to influence genesis frequency[73]. Thus, vorticity may have an outsized influence on GPI at high latitudes, where vorticity is usually higher than that threshold. Additionally, $\chi$ and vorticity do not appear to contribute skill in replicating inter-annual variability in tropical cyclogenesis in modern climate, at least in the Atlantic Ocean[71]. We focused our analysis on GPI, which includes the influences of both vorticity and χ, because while they may not contribute substantially to inter-annual variability in tropical cyclogenesis in the relatively stable modern climate, over centennial timescales and in climate states warmer or cooler than modern climate they may have greater influence. However, it is also possible that they could introduce unrealistic centennial variability in GPI. To test the robustness of our climate model analysis to the exclusion of vorticity and χ, we also calculated the cyclone genesis index (CGI) of Bruyere et al.[71], which includes only vertical wind shear and potential intensity as inputs.

$$CGI = (PI/70)^3\,(1 + 0.1V_{shear})^{-2}$$

We found that the differences in CGI between the MCA and the LIA were qualitatively similar to those in GPI (ED Fig. 6).

**Supplementary References**

62. Holmes, C.W. $\delta^{18}O$ variations in the *Halimeda* of Virgin Islands sands: Evidence of cool water in the Northeast Caribbean, Late Holocene. *J. Sediment. Petrol.* **53**: 0429-0438 (1983).

63. Xu, H.et al. Biogenic carbonate formation and sedimentation in the Xisha Islands: evidences from living *Halimeda*. *Acta Oceanol. Sin.* **34**: 62-73 (2015).

64. Chen, T., Roff, G., Feng, Y., and Zhao, J. Tropical sand cays as natural paleocyclone archives. *Geophys. Res. Lett.* **46**: 9796-9803 (2019).

65. Dietrich, W.E. Settling velocity of natural particles. *Water Resour. Res.* **18**, 1615-1626 (1982).

66. Kench, P.S. and McLean, R.F. Hydraulic characteristics of bioclastic deposits: new possibilities for environmental interpretation using settling velocity fractions. *Sedimentology* **43**, 561-570 (1996).

67. Braithwaite, C.J.R. Settling behaviour related to sieve analysis of skeletal sands. *Sedimentology* **20**, 251-262 (1973).

68. Maiklem, W.R. Some hydraulic properties of bioclastic carbonate grains. *Sedimentology* **10**, 101-109 (1968).

69. Spennemann, D.H.R. and Marschner, I.G. Stormy years: On the association between the El Nino/Southern Oscillation phenomenon and occurrence of typhoons in the Marshall Islands. Report to the Federal Emergency Management Agency Region 9, Albury, Australia (1994).

70. Camargo, S.J., Robertson, A.W., Gaffney, S.J., Smyth, P., and Ghil, M. Cluster analysis of typhoon tracks. Part I: General properties. *J. Climate* **20**, 3635-3653 (2007).

71. Bruyere, C.L., Holland, G.J., and Towler, E. Investigating the use of a genesis potential index for tropical cyclones in the North Atlantic basin. *J. Climate* **25**, 8611-8626 (2012).

72. Camargo, S.J., Sobel, A.H., Barnston, A.G., Emanuel, K.A. Tropical cyclone genesis potential index in climate models. *Tellus* **59A**, 428-443 (2007).

73. Tippett, M.K., Camargo, S.J., and Sobel, A.H. A Poisson regression index for tropical cyclone genesis and the role of large-scale vorticity in genesis. *J. Climate* **24**, 2335-2357 (2011).